FOCUS ISSUE

ADVANCED NANOMECHANICAL TESTING

The indentation size effect of single-crystalline tungsten revisited

Jin Wang[1,2], **Tillmann Volz**[3,4], **Sabine M. Weygand**[4], **Ruth Schwaiger**[1,2,5,a)]

[1] Institute for Applied Materials, Karlsruhe Institute of Technology (KIT), Karlsruhe, Germany
[2] Institute of Energy and Climate Research, Forschungszentrum Juelich GmbH, Juelich, Germany
[3] Center of Applied Research, Karlsruhe University of Applied Sciences, Karlsruhe, Germany
[4] Faculty of Mechanical Engineering and Mechatronics, Karlsruhe University of Applied Sciences, Karlsruhe, Germany
[5] Chair of Energy Engineering Materials, RWTH Aachen University, Aachen, Germany
a) Address all correspondence to this author. e-mail: r.schwaiger@fz-juelich.de

In this study, we have investigated the indentation size effect (ISE) of single crystalline tungsten with low defect density. As expected, the hardness shows a pronounced increase with decreasing indentation depth as well as a strong strain rate dependence. For penetration depths greater than about 300 nm, the ISE is well captured by the Nix–Gao model in the context of geometrically necessary dislocations. However, clear deviations from the model are observed in the low depth regime resulting in a bilinear effect. The hardness behavior in the low depth regime can be modeled assuming a non-uniform spacing of the geometrically necessary dislocations. We propose that the bilinear indentation size effect observed reflects the evolution of the geometrically necessary dislocation density. With increasing strain rate, the bilinear effect becomes less pronounced. This observation can be rationalized by the activation of different slip systems.

Introduction

The indentation size effect (ISE) describes the observation that the hardness of a material increases as the size of an indent decreases [1]. The ISE has been known for many years, mostly noticed in crystalline materials with low defect density indented with pyramidal indenters, and becomes particularly important at depths below 1 μm. It has indeed been observed for a range of different materials, e.g., Cu, Ag, Ir, MgO and W [2–10]. Those experimental reports indicate that the ISE is neither related to the crystal structure, nor alloying elements, but rather caused by the pronounced strain gradients in the stress field under the indenter tip at small indentation depths [1]. However, while the overall trend in experiments is comparable, different characteristics of the ISE in particular in the low depth regime have been reported. Several models were suggested that describe the ISE mathematically [4, 9, 11–13], among which the Nix–Gao model [11] is probably the most widely discussed one. In the following, we will briefly summarize its main ideas.

The plastic flow in the indented region does not solely depend on the strain state but also on the gradients of strain, which are associated with the geometrically necessary dislocations (GNDs) that arise from the geometry of the indenter tip as it penetrates into the sample. Since strain gradients are inversely proportional to a length scale [14, 15], i.e. the depth of indentation, the influence of strain gradients (and of the GNDs) becomes more pronounced when the indentation depth is reduced. For higher depths, the strain gradients in the deformed volume decrease and become insignificant. By contrast, the statistically stored dislocations (SSDs) are usually randomly distributed in a material and formed through uniform straining, e.g., during processing of the material.

Based on the Taylor relation [16], the hardness H of a material is proportional to the flow stress σ, which can be expressed by the following equation [11, 16] relating H to the dislocation density ρ:

$$H = 3\sigma = 3\sqrt{3}\alpha\mu b\sqrt{\rho}, \tag{1}$$

with α as a constant characteristic of the dislocation structure, μ the shear modulus and b the magnitude of the Burgers vector of a material. According to strain gradient plasticity [14, 15], the increased size-dependent hardness value should be ascribed to

the increased density of GNDs, while the depth-independent, macroscale hardness value H_0 would be related to the constant density of the SSDs. Therefore, Eq. (1) can be rewritten as [11]

$$H = 3\sigma = 3\sqrt{3}\alpha\mu b\sqrt{\rho_S + \rho_G}, \tag{2}$$

where ρ_S and ρ_G are the densities of the SSDs and GNDs, respectively.

Based on strain gradient plasticity, Nix and Gao assumed that the GNDs are concentrated uniformly beneath a conical indenter tip in a hemispherical volume $V = 2/3\pi a^3$, the size of which is defined by the contact radius a of the indenter tip. Based on these assumptions, the total length of the dislocation loops and the dislocation density can be determined. In order to calculate the GND density, Nix and Gao assumed a hemispherical volume, in which the GNDs are closely packed [11] and the distribution of the dislocation loops in the deformed volume is assumed as homogeneous. Thus, the spacing between the slip steps is constant. The GND density ρ_G is described [11] as:

$$\rho_G = \frac{\lambda}{V} = \frac{3h}{2ba^2} = \frac{3}{2bh}\tan^2\theta. \tag{3}$$

with θ as the contact angle of the indenter tip and h the indentation depth.

The Nix–Gao model describes a linear relation between the square of the hardness H^2 and the inverse indentation depth $1/h$ [11]

$$H^2 = H_0^2 + H_0^2 \cdot \frac{h^*}{h}, \tag{4}$$

with the depth-independent hardness

$$H_0 = 3\sqrt{3}\alpha\mu b\sqrt{\rho_S} \tag{5}$$

and the material characteristic length scale

$$h^* = \frac{81}{2}b\alpha^2\tan^2\theta\left(\frac{\mu}{H_0}\right)^2. \tag{6}$$

The Nix–Gao model has been applied to various materials and has been demonstrated to capture the ISE over depths ranging from several micrometers to some hundred nanometers [1, 11]. However, with the improvement of the nanoindentation instrumentation, even lower indentation depths became accessible, and the classic model revealed some shortcomings when the indentation depths were reduced to < 300 nm [1, 4, 9]. At such small depths, the Nix–Gao model overestimates the hardness values of several materials, as shown in Fig. 1. The experimental results of a number of studies [2–10, 17] are summarized and compared with the Nix–Gao model [11]. Focusing on the "break-down" of the Nix–Gao model [1], some modifications of the model were suggested [4, 9, 12, 13].

In this study, we focused on understanding the ISE of single-crystalline tungsten. While single-crystalline tungsten serves as
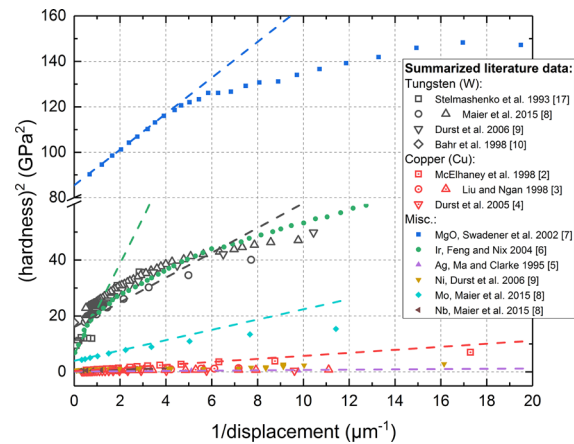

Figure 1: The ISE has been observed for a wide range of different materials [2–10, 17]. In the higher depth regime, the plot of the experimental results according to the Nix–Gao model [11] shows in general good agreement with the model prediction (dashed lines, Eq. 4).

a model material, tungsten and tungsten alloys are also of high technological relevance. They have outstanding mechanical and physical properties at high temperatures [18, 19], and therefore, great potential as structural materials in high-temperature energy conversion systems. However, as the brittle-to-ductile transition temperature of tungsten is fairly high [20, 21], the brittleness at room temperature limits its applicability. Furthermore, the mechanical behavior of tungsten is strongly affected by its microstructures, i.e. the crystal orientations, the grain size, and the shape of the grains [20, 22–28]. Thus, a comprehensive understanding of the deformation mechanisms at room temperature on the microscale and in particular of material size effects is indispensable both with regard to the application and our fundamental understanding of deformation.

Here, (001) tungsten was comprehensively characterized using different indentation methods and indentation strain rates with a particular focus on the low depth regime. The data was analyzed in the context of the Nix–Gao model assuming that the dislocation spacing in the deformed volume is no longer uniform. The implications of this description on the deformation mechanisms and the ISE will be discussed.

Results and discussion

Indentation behavior of single-crystalline tungsten

The indentation behavior of single-crystalline W was determined using different nanoindentation methods over a range of indentation strain rates. Typical load-displacement curves of (001) W are shown in Fig. 2. Both quasi-static and dynamic indentation experiments were performed and the load-displacement curves show good agreement.
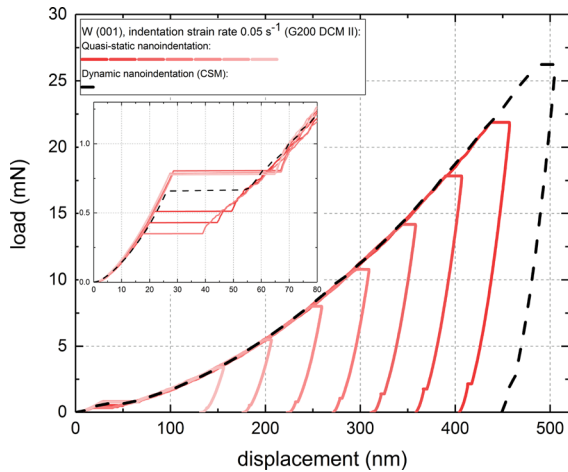
Figure 2: Typical load-displacement curves of (001) W obtained using quasi-static and dynamic testing methods. The pop-ins at indentation depths < 50 nm indicate the transition from elastic to plastic deformation, shown in greater detail in the inset. No difference in pop-in behaviors was observed for different test methods used.

The hardness values of the (001)-oriented single crystal are shown in Fig. 3, together with the results of previous studies of tungsten [8, 9]. Since we are not analyzing the transition from elastic to plastic deformation shown as pop-ins in the load–displacement curves (Fig. 2) , e.g. [9], the hardness data are only shown in the depth regime from 100 to 2000 nm in Fig. 3.
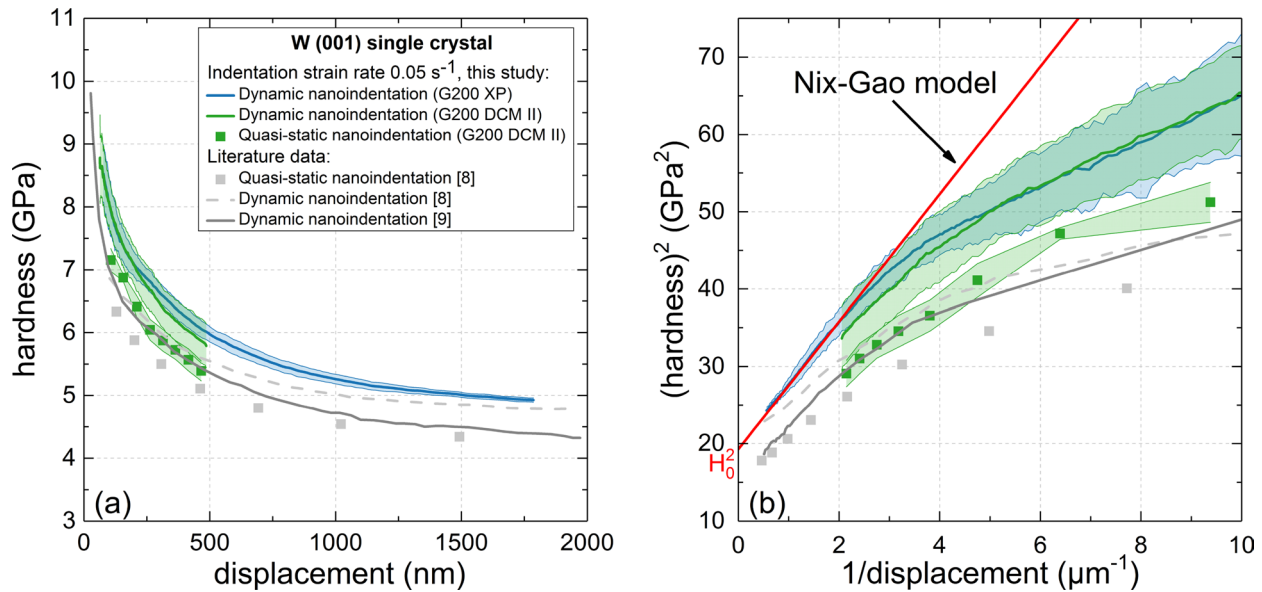
Both the hardness values of this work and the literature data show a pronounced ISE following the same trend. The different indenter modules, i.e. XP and DCM II heads, do not affect the hardness values, indicated by the overlap of the blue and green bands. The dynamic and the quasi-static hardness data reveal the same trend of the ISE, while the quasi-static hardness data are lower (green symbols in Fig. 3). The lower hardness values can be explained by a reduced effective strain rate of the quasi-static measurements [29]. This effect can also be seen in the data set of the quasi-static and dynamic data of [8] shown as grey squares and grey line in Fig. 3, respectively. The effective strain rate was determined as 0.033 s^{-1} [8], which results in the smaller hardness values compared to the other data at the indentation strain rate of 0.05 s^{-1} [8, 9]. In Fig. 3b, all data sets reveal a significant bilinear behavior of H^2 vs. $1/h$; the hardness in the low depth regime (<300 nm) cannot be described by the Nix–Gao model, as indicated by the red line. A transition regime occurs in the bilinear hardness behavior at depths around 300 nm, which is independent of the indenter module or indentation method. Similarly, bilinear behavior with a transition at comparable depths was observed on some other materials [2–4, 6–9, 17], as shown in Fig. 1. In this study, such bilinear indentation behavior did not only occur at the indentation strain rate of 0.05 s^{-1}. In Fig. 4, the hardness data determined at nine different strain rates are shown as H versus h and H^2 versus $1/h$ exhibiting similar behaviors.

Figure 3: Indentation size effect of (001) W: (a) Hardness vs. displacement, and (b) Nix–Gao plot H^2-$1/h$. The blue and green lines represent the averaged hardness of the dynamic measurements using the G200 XP and DCM II. Results from the quasi-static indentation experiments are denoted by the green squares. The standard deviations are shown as blue- and green-shaded areas. Note, that the different size of the data sets, i.e. 20 for XP and 6 for each DCM II measurement series may cause differences in the standard deviations. The red line is the model prediction of the dynamic data. From the intercept with the ordinate, the H_0 is determined [11]. For comparison, hardness data of previously published studies [8, 9] have been added and are shown as grey lines and symbols.
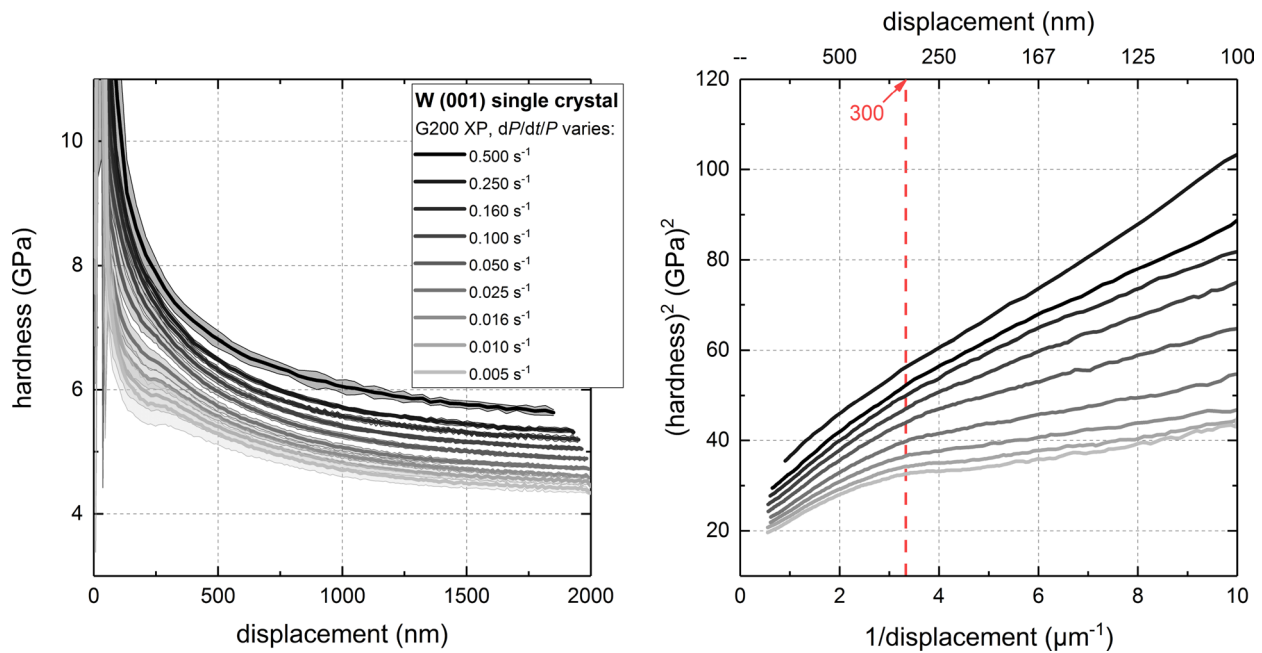
Figure 4: The hardness of the (001) W single crystal exhibits a pronounced strain rate dependence: (a) Hardness vs. displacement at nine different indentation strain rates, and (b) the corresponding Nix–Gao plot $H^2 - 1/h$. The mean values are shown as solid lines with the standard deviations as gray shaded areas. The color density of the lines decreases with decreasing strain rate.

Generally, the hardness values increase with increasing strain rate, which is expected due to the strain rate sensitivity of single crystalline tungsten [8]. A significant ISE is observed in all the experimental data sets. At the maximum depth of $\sim$ 2000 nm, the depth-independent hardness values H_0 have not yet been reached. Therefore, the depth-independent hardness H_0 is determined from an extrapolation of the fitted curve (see red line in Figure 3). For the different strain rates, the H_0 values are in the range from 3.98 GPa to 5.10 GPa, showing good agreement with the literature [9, 10].

The bilinear behavior of H^2 versus $1/h$ is visible at all strain rates varying from 0.005 to 0.5 s^{-1} (Fig. 4b). However, the higher the strain rate, the less pronounced the bilinear effect. In all indentation data sets, the transition of the two depth regimes occurs at a similar depth around 300 nm (see the red dashed line in Fig. 4b), while the transition depth appears to be shifted towards smaller depths when the strain rate increases. Furthermore, the curves at the different strain rates are not parallel. For example, the difference of the hardness values at two strain rates at the highest depths is smaller than the difference in the low depth regime, for instance at 200 nm. Such bilinear behavior was confirmed for a (112) tungsten single-crystal (data not shown here), which will be discussed further below.

Modeling of the bilinear indentation size effect

As shown in Figs. 3 and 4, our experiments revealed a clear bilinear behavior and an overestimation of the hardness values

using the Nix–Gao description. Such an overestimation in the low depth regime could be related to the dynamic measurement [30–32] or a blunt tip [9]. However, the same effect was observed for quasi-static indentation experiments (Fig. 3), and the transition regime at a depth of $\sim$300 nm is not affected by a blunt tip since the pop-ins, i.e. the transition from a Hertzian contact to the Berkovich indentation, was observed at a depth of $\sim$20 nm. A non-linear ISE has indeed been observed for bcc metals before [13] and was suggested to be related to the non-negligible internal friction stress, namely the Peierls stress [13]. However, accounting for the Peierls stress within the framework of strain gradient plasticity, the relation of H^2-$1/h$ becomes parabolic, instead of linear [13], which does not capture the bilinear behavior observed in this study.

The Nix–Gao model is based on two fundamental assumptions [11]: (1) the GNDs are concentrated in a hemispherical volume of the same radius a as the projected contact area, and (2) the GNDs are distributed uniformly and close-packed in the volume resulting in a constant dislocation spacing s. These two assumptions, though, can hardly be fulfilled at the same time [1, 7]. Therefore, either the GND volume needs to be extended, or the GND density needs to change continuously over the volume during the indentation process from the maximum to approximately zero. For the case of the extended GND volume, Durst et al. [4, 9] assumed a factor f to describe the extension of the plastic zone. This factor f, however, needs to be determined from the hardness data, and cannot describe the bilinear ISE. By contrast, a gradient of GND density distribution underneath the

indents was indeed observed in transmission electron microscopy and electron backscatter diffraction studies [33–37].

In the following, we assume that the GND spacing $s(r)$ is non-uniform and depends on the position r away from the center of the indent as schematically shown in Fig. 5a. In addition, we assume that $s(r)$ reaches the minimum at the center of the indent, and is equal to the constant dislocation spacing s of the Nix–Gao model (shown schematically in Fig. 5c). Accordingly, the density of GNDs in Fig. 5a would decrease from the center to the edge of the indent. Therefore, $s(r)/s$ should fulfill the following boundary conditions:

$$\frac{s(r)}{s} = \begin{cases} 1, & \text{for } r = 0, \\ +\infty, & \text{for } r = a \end{cases} \tag{7}$$

Assuming the increase of $s(r)$ is continuous,

$$\frac{s(r)}{s} = \frac{a}{a - r} \tag{8}$$

and by substituting the constant $s = b/\tan\theta$ into the last equation, Eq. (8) can be rewritten as

$$s(r) = \frac{a}{(a - r)} \frac{b}{\tan\theta} \tag{9}$$

It should be noted that Eq. (9) is the same as Eq. (22) in the original paper by Nix and Gao [11], in which a constant strain gradient was assumed already noticing the potential limitations of the original assumptions. According to [11], the dislocation spacing would no longer be uniform, when a constant strain gradient would be sustained.

The total length of the injected dislocation loops $\lambda(r)$ with respect to the position-dependent dislocation spacing can be calculated as

$$\lambda(r) = \int_0^a d\lambda(r) = \int_0^a 2\pi r \frac{dr}{s(r)} = \frac{\pi h a}{3b} \tag{10}$$

Analogous to the Nix–Gao model, $d\lambda(r)$ is the length of the loop located between the position r to $r + dr$. The diluted GND density according to this adapted model is then determined as:

$$\rho_{\text{G, diluted}} = \frac{1}{2bh} \frac{\tan^2\theta}{} \tag{11}$$
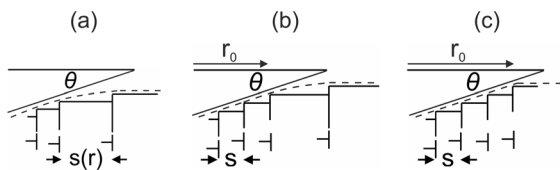

(a)   (b)   (c)

Figure 5: Schematic of the GND distribution from the (a) low depth regime to (c) the high depth regime. In (a), the GND distribution fulfills the adapted model describing the diluted GND density while (c) illustrates the classic Nix–Gao model. A combination of these two behaviors is shown in (b). In this case, the saturated volume is described by the radius r_0.

Compared to the original Nix–Gao model, the GND density of this adapted model is reduced to one-third of ρ_G in Eq. (3). Accordingly, the material characteristic length scale is also reduced:

$$h^*_{\text{diluted}} = \frac{27}{2} b\alpha^2 \tan^2\theta \left(\frac{\mu}{H_0}\right)^2 \tag{12}$$

Thus, the slope of the H^2-$1/h$ behavior predicted by the adapted model should be one third of the prediction of the Nix–Gao model.

The description above, describes a GND volume that is not yet saturated. The assumption of non-uniformity does not only yield a reduced GND density, but the description of GND distribution might also be more realistic for the low depth regime, where the deformation zone is significantly affected by the elastically deformed material and full contact has not yet been achieved. With increasing depth more material in the center has to deform to adapt to the tip geometry until full contact is achieved. The central part underneath the indent will be filled with GNDs eventually and the saturated state will be reached fulfilling the description of the Nix–Gao model. In Fig. 5, such an evolution process of the GND distribution in the different depth regimes is schematically illustrated. Such a dynamical picture was recently shown experimentally for tungsten [38]. Javaid et al. [38] compared the GND structures beneath the indents to different loads using high resolution electron backscatter diffraction. They observed a gradual decrease of the GND density from the indent center to the edge at a lower load, i.e. a smaller depth, while the GND density appeared more evenly distributed at a higher load. Also wedge indentation of tungsten single crystals in combination with transmission Kikuchi diffraction analysis of cross sections through indents revealed differences in the dislocation structures [39].

Assuming the transition between the two depth regimes occurs at the depth of h_0, the bilinear model can be mathematically described as:

$$H^2 = \begin{cases} H_0^2 + H_0^2 \cdot \frac{h^*}{h} & \text{when } h \geq h_0 \\ H_0^2 + H_0^2 \cdot \frac{2}{3} \cdot \frac{h^*}{h_0} + H_0^2 \cdot \frac{1}{3} \cdot \frac{h^*}{h} & \text{when } h < h_0 \end{cases} \tag{13}$$

with h^* the same as in the Nix–Gao model shown in Eq. (6).

Validation of the bilinear ISE model

The bilinear model will be validated by comparing the experimental data of two tungsten single crystals, i.e. (001) and (112) orientations. The mean values of H^2-$1/h$ of both orientations are shown in Fig. 6 determined at the indentation strain rate of 0.05 s^{-1}. The suggested bilinear model in Eqs. (13) and (6) has been fitted to the experimental data and is indicated by the dashed red lines. For the (001) crystal, the dislocation core parameter α
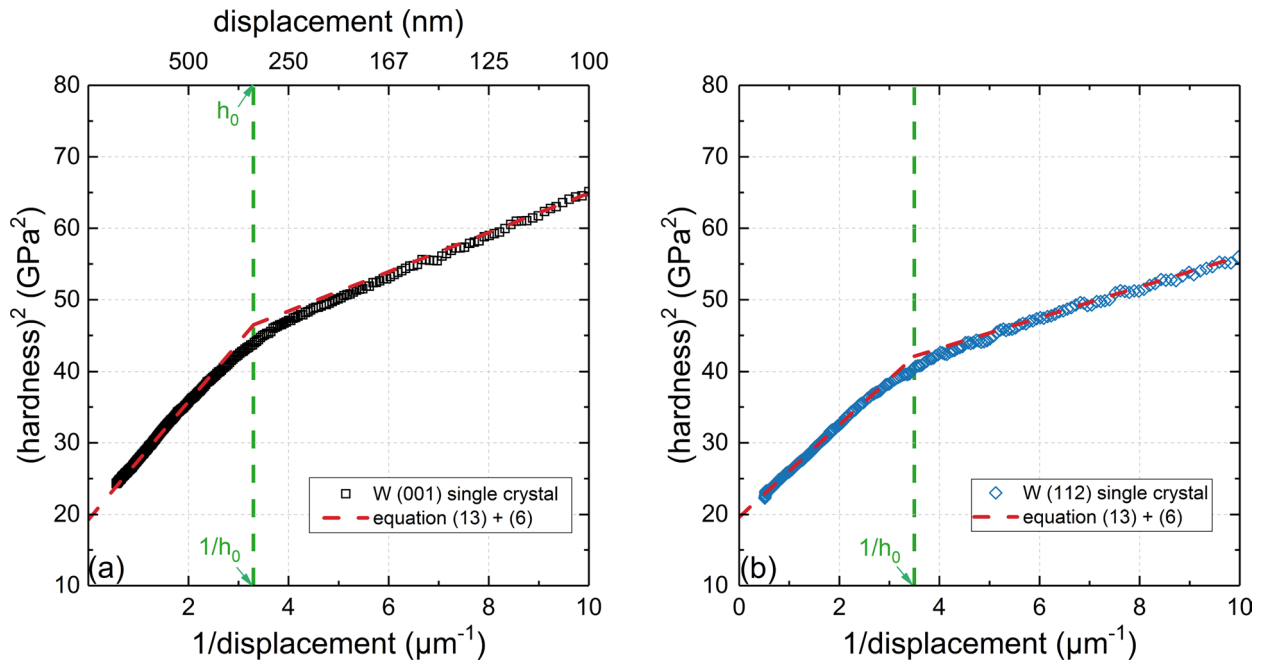
2170

Figure 6: The ISE was observed for both (a) the (001) and (b) the (112) W single crystals. The Nix–Gao plots reveal the bilinear ISE, which can be described by the model in Eqs. (13) and (6). The average hardness values of 20 indents for each crystal orientation are shown. For the (001) W crystal, H_0 and h_0 were determined as 4.39 GPa and 303 nm, respectively, and for the (112) crystal as 4.43 GPa and 286 nm.

was assumed as 0.5 [4, 9, 11]. For the (112) orientation, $\alpha = 0.44$ resulted in a better match of the model to the experimental data. Other parameters, such as the Burgers vector b, shear modulus μ and equivalent tip angle θ are constant and determined by the material and tip geometry. The parameters H_0, h^* and h_0 in Eqs. (13) and (6) were determined as follows: hardness data in the high depth regime from 500 nm to 2000 nm were fitted by the original Nix–Gao model, yielding H_0. Then, h^* was calculated according to Eq. (6). Subsequently, h_0 was estimated using the hardness data in the low depth regime from 100 nm to 200 nm using Eq. (13). The ISE as described by the bilinear model is shown as H^2 versus $1/h$ in Fig. 6 (red dashed line). It captures the experimental behavior of both crystal orientations. The transition between the two depth regimes occurs at h_0 (green dashed lines in Fig. 6a and b).

The experimental results of the (001) and (112) oriented single crystals can be well described by the bilinear ISE model. However, one might argue that the transition of the two depth regimes of the (001) crystal can rather occur in a depth range than a certain depth. As shown in Fig. 6a, the transition regime ranges from ~250 nm to ~350 nm. Near the transition depth h_0, the two regimes have to overlap since the deformed volume is occupied by dislocations gradually when the deformation proceeds, and the predominant GND mechanism has to change, as illustrated in Fig. 5b.

In the mixed state of two GND mechanisms, however, the effects of the diluted (Fig. 5a) and saturated GND distributions

(Fig. 5c) should not be neglected. This mixed state can be described assuming a smaller hemispherical volume of radius r_0 in which the GNDs are closely packed surrounded by a GND distribution following the description in Fig. 5a. For $h>h_0$, the dense GND volume starts to dominate. Thus:

$$\frac{h - h_0}{r_0} \approx \frac{h}{a} = \tan \theta. \tag{14}$$

From $r = 0$ to r_0, the GND spacing is equal to s, and the total length of dislocation loops λ_1 is

$$\lambda_1 = \int_0^{r_0} 2\pi r \frac{\mathrm{d}r}{s} = \frac{\pi(h - h_0)r_0}{b} \tag{15}$$

while from r_0 to a, the dislocation spacing $s_2(r)$ is non-uniform, and can be described as

$$\frac{s_2(r)}{s} = \frac{a - r_0}{a - r_0 - (r - r_0)} = \frac{a - r_0}{a - r} \tag{16}$$

Therefore, the length of the loops $\lambda_2(r)$ from r_0 to a is calculated as

$$\lambda_2(r) = \int_{r_0}^{a} 2\pi r \frac{a - r}{a - r_0} \frac{h}{ab} \mathrm{d}r = \frac{\pi(h - h_0)}{3r_0 b}(a^2 + ar_0 - 2r_0{}^2) \tag{17}$$

Defining $n = r_0/a$ for the proportion of the saturated volume to the total GND volume and according to Eq. (14), $n \approx (h - h_0)/h$. The total dislocation length is then calculated:

$$\lambda_{\text{mixed}} = \lambda_1 + \lambda_2(r) = \frac{\pi(h-h_0)}{3b}\left(r_0 + \frac{a^2}{r_0} + a\right)$$

$$= \frac{\pi(h-h_0)a}{3b}\left(n + 1 + \frac{1}{n}\right) \qquad (18)$$

$$= \frac{\pi ha}{3b}(n^2 + n + 1)$$

The GND density for the mixed state is

$$\rho_{\text{G, mixed}} = \frac{1}{2bh}\frac{\tan^2\theta}{}(n^2 + n + 1) \qquad (19)$$

and the material characteristic length scale

$$h^*_{\text{mixed}} = \frac{27}{2}b\alpha^2 \tan^2\theta\left(\frac{\mu}{H_0}\right)^2(n^2 + n + 1)$$
$$= \frac{1}{3}h^*(n^2 + n + 1). \qquad (20)$$

Note, that the slope in the transition regime equals to $H_0^2 \cdot h^*_{\text{mixed}}$ and is described as a function of h, as $n \approx (h - h_0)/h$. Therefore, the model introduced in this section, captures the ISE over the whole depth range after the pop-in. As can be seen in Eq. (20), if r_0 approaches zero, h^*_{mixed} gives the same result as in Eq. (13) for the small depth regime. By contrast, when the volume filled with the saturated GND density is large and r_0 approaches a, h^*_{mixed} approaches the description of the high depth regime in Eq. (13).

In Fig. 7, the bilinear model including the mixed state of the two GND mechanisms has been applied to the hardness values of the (001) single crystal. In the depth range from 230 nm to 370 nm, the gradual transition between the two depth regimes can be be well characterized.

The transition regime of the ISE behavior becomes more pronounced, when the strain rate increases (Fig. 4) and the bilinear behavior is therefore less apparent. In Fig. 8, the bilinear model in Eqs. (13), (6) and (20) is compared with the experimental data at three strain rates, i.e. 0.5 s^{-1}, 0.05 s^{-1}, and 0.005 s^{-1}.

With increasing strain rate, the bilinear behavior becomes less significant. The ISE at the lower strain rates, i.e. 0.05 s^{-1} and 0.005 s^{-1}, can be well described by Eqs. (13) and (6) (Fig. 8). While the ISE behavior at the highest strain rate of 0.5 s^{-1} still appears bilinear, the behavior in the low depth regime is better described by Eqs. (13) and (20) considering the occurrence of the two GND mechanisms as depicted in Fig. 5b.

In addition, as shown in Fig. 4, the H^2-$1/h$ curves at the different strain rates are not parallel. The slope of the H^2-$1/h$ behavior increases with increasing strain rate, in both the low and high depth regimes. The slope of the H^2-$1/h$ behavior Δ can be written as:

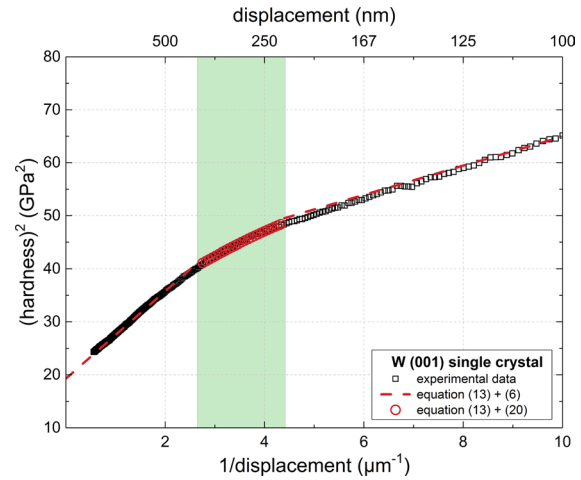$$\Delta = H_0^2 \cdot h^* = \frac{81}{2}b\alpha^2 \tan^2\theta\mu^2 \qquad (21)$$

Figure 7: Indentation size effect of (001) tungsten single crystal. The average of 20 indents is shown together with the bilinear model described by Eqs. (13) and (6). In addition, the transition regime of the mixed state is considered and described by Eqs. (13) and (20). The transition regime was determined over the depth ranging from 230 nm to 370 nm.
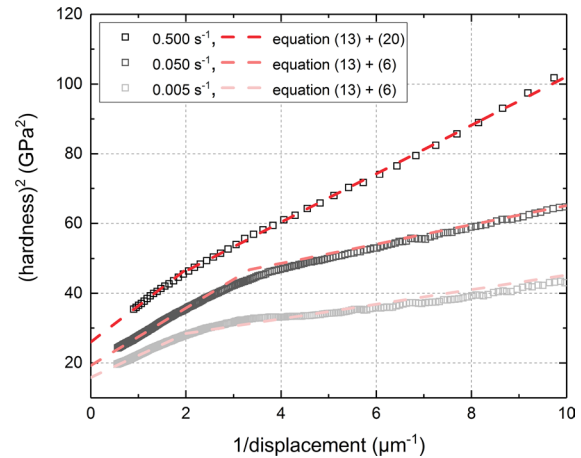

Figure 8: Bilinear ISE at three different strain rates. Average data of 20 indents at each strain rate are shown together with the ISE model described by Eqs. (13), (6) and (20).

which does not depend on the depth-independent hardness H_0^2. The other quantities, i.e. the Burgers vector b, the contact angle θ and the shear modulus μ are independent of the strain rate, which indicates that the the parameter α depends on the strain rate. According to the literature [11, 40, 41], α describes the dislocation core structure. For single-crystalline tungsten, when the crystal orientation or the indentation strain rate varies, α may vary as the dislocation structures might be different. Evidence can be seen in Fig. 6, which shows that rather $\alpha = 0.44$ than 0.5 describes the indentation behavior of the (112) orientation.

The proper values of the parameter α at the nine indentation strain rates are determined from the experimental data in the

depth range from 500 nm to 2000 nm, according to Eq. (21). The values are plotted over the strain rate in Fig. 9. With the indentation strain rates increasing from 0.005 s^{-1} to 0.5 s^{-1}, the α values of (001) W increase slightly in the range from 0.4 to 0.6. For the strain rate of 0.05 s^{-1}, the fitted α of 0.50 coincides with the literature value [9, 11]. The strain rate dependence of α is likely related to the activation of different slip systems or a variation of the dislocation types involved.

Summary

Nanoindentation experiments were conducted on (001) and (112) tungsten single crystals using different indentation methods to study the indentation size effect. Both crystal orientations exhibit a significant bilinear behavior of H^2 versus $1/h$, which was observed over a range of different indentation strain rates. The increase of the hardness with decreasing depth cannot be described by the Nix–Gao model [11] over the full depth range. The overestimation of the Nix–Gao model in the low depth regime can be resolved using the assumption of a diluted GND distribution at low indentation depth. We suggest that the bilinear behavior reflects the development of the GND structure from a non-uniform distribution or diluted density to the saturated state captured by the Nix–Gao model. In this picture, the transition region in the H^2 versus $1/h$ curves between the two depth regimes would be related to the combination of the two behaviors. With increasing strain rate the bilinear behavior is less obvious. At the higher indentation strain rates, the mixed state of the two GND mechanisms has to be taken into consideration and explains the transition regime observed. As the parameter α, which is characteristic of the dislocation structures, is strai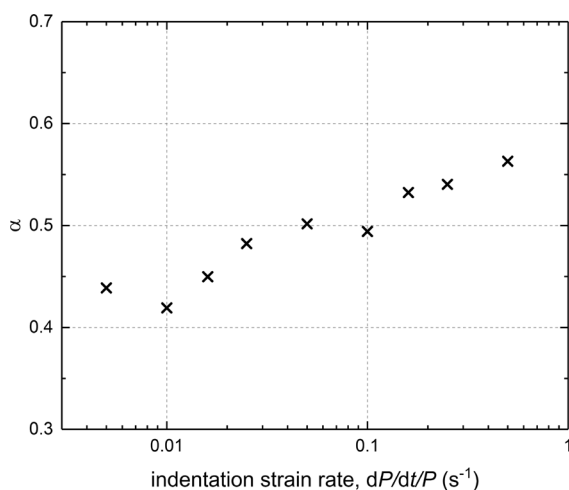n rate dependent, we argue that the effect of the strain rate on the bilinear behavior is related to a change of the glide systems involved. This is corroborated by the change of α for different crystal orientations.

Materials and methods

Single-crystalline tungsten with two different out-of-plane orientations was studied. The samples were mechanically ground and polished using SiC paper and diamond suspensions down to a grain size of 1 μm. The final mechanical polishing step was conducted using OP-A (acidic alumina) with 0.06 μm grain size. Finally, the samples were electrolytically polished (LectroPol, Struers GmbH, Willich, Germany) using 2 wt% NaOH solution with a voltage of 10 V for 30 s. The preparation procedure resulted in a final surface roughness R_a of 0.009 μm, measured over an area of ∼2.5 × 2.5 μm^2 using a laser scanning confocal microscope (VK-9710K, Keyence Corporation, Osaka, Japan). The out-of-plane orientations of the single crystals were confirmed as (001) and (112) by electron backscatter diffraction [42].

The nanoindentation experiments were conducted using a Nanoindenter G200 (Agilent/Keysight Technologies, Inc., California, USA) equipped with a diamond Berkovich tip. Both dynamic and quasi-static indentation experiments were performed to detect a potential effect of the indentation method on the hardness values [29, 43]. Constant strain rate (CSR) experiments to a depth of 2000 nm were conducted at nine different indentation strain rates ranging from 0.005 to 0.5 s^{-1} using the XP head of the G200. At each strain rate, 20 indents were performed. Here, the indentation strain rate $\dot\varepsilon$ is defined as [44]:

$$\dot\varepsilon = \frac{\dot P}{P} \tag{22}$$

with P as the load on the sample.

In the low depth regime (up to 500 nm), in addition, 6 indents under each condition were conducted using the DCM II head. For the dynamic measurements, frequency and displacement amplitude were set to 45 Hz and 2 nm for the XP head and 75 Hz and 1 nm for the DCM head, respectively.

Acknowledgments

Figure 9: The value of α of the (001) single crystal over indentation strain rates from 0.005 to 0.5 s^{-1}. Note the logarithmic scale of the x axis.

State Physics (RAS, 142432 Chernogolovka Moscow District, Russia).

Data availability

Data will be made available upon reasonable request.

Declarations

Conflict of interest The authors declare no conflict of interests.

Supplementary Information

The online version contains supplementary material available at https://doi.org/10.1557/s43578-021-00221-6.

References

1. G.M. Pharr, E.G. Herbert, Y. Gao, The indentation size effect: a critical examination of experimental observations and mechanistic interpretations. Annu. Rev. Mater. Res. **40**, 271–292 (2010)

2. K. McElhaney, J.J. Vlassak, W.D. Nix, Determination of indenter tip geometry and indentation contact area for depth-sensing indentation experiments. J. Mater. Res. **13**, 1300–1306 (1998)

3. Y. Liu, A.W. Ngan, Depth dependence of hardness in copper single crystals measured by nanoindentation. Scripta Mater. **44**, 237–241 (2001)

4. K. Durst, B. Backes, M. Göken, Indentation size effect in metallic materials: correcting for the size of the plastic zone. Scripta Mater. **52**, 1093–1097 (2005)

5. Q. Ma, D.R. Clarke, Size dependent hardness of silver single crystals. J. Mater. Res. **10**, 853–863 (1995)

6. G. Feng, W.D. Nix, Indentation size effect in MgO. Scripta Mater. **51**, 599–603 (2004)

7. J. Swadener, E. George, G. Pharr, The correlation of the indentation size effect measured with indenters of various shapes. J. Mech. Phys. Solids **50**, 681–694 (2002)

8. V. Maier, C. Schunk, M. Göken, K. Durst, Microstructure-dependent deformation behaviour of bcc-metals-indentation size effect and strain rate sensitivity. Philos. Mag. **95**, 1766–1779 (2015)

9. K. Durst, B. Backes, O. Franke, M. Göken, Indentation size effect in metallic materials: modeling strength from pop-in to macroscopic hardness using geometrically necessary dislocations. Acta Mater. **54**, 2547–2555 (2006)

10. D.F. Bahr, D. Kramer, W. Gerberich, Non-linear deformation mechanisms during nanoindentation. Acta Mater. **46**, 3605–3617 (1998)

11. W.D. Nix, H. Gao, Indentation size effects in crystalline materials: a law for strain gradient plasticity. J. Mech. Phys. Solids **46**, 411–425 (1998)

12. Y. Huang, F. Zhang, K. Hwang, W. Nix, G. Pharr, G. Feng, A model of size effects in nano-indentation. J. Mech. Phys. Solids **54**, 1668–1686 (2006)

13. X. Qiu, Y. Huang, W. Nix, K. Hwang, H. Gao, Effect of intrinsic lattice resistance in strain gradient plasticity. Acta Mater. **49**, 3949–3958 (2001)

14. N. Fleck, G. Muller, M.F. Ashby, J.W. Hutchinson, Strain gradient plasticity: theory and experiment. Acta Metall. Mater. **42**, 475–487 (1994)

15. J. Hutchinson, N. Fleck, Strain gradient plasticity. Adv. Appl. Mech. **33**, 295–361 (1997)

16. G.I. Taylor, The mechanism of plastic deformation of crystals. Part I - theoretical. Proc. R. Soc. Lond. A **145**, 362–387 (1934)

17. N. Stelmashenko, M. Walls, L. Brown, Y.V. Milman, Microindentations on W and Mo oriented single crystals: an SEM study. Acta Metall. Mater. **41**, 2855–2865 (1993)

18. J.R. Stephens, Review of deformation behavior of tungsten at temperature less than 0.2 absolute melting temperature, NASA Technical Memorandum TM X-2482 (1972)

19. E. Lassner, W.-D. Schubert, *Tungsten: Properties, Chemistry, Technology of the Element, Alloys, and Chemical Compounds* (Springer, Boston, 1999).

20. P. Gumbsch, J. Riedle, A. Hartmaier, H.F. Fischmeister, Controlling factors for the brittle-to-ductile transition in tungsten single crystals. Science **282**, 1293–1295 (1998)

21. P. Gumbsch, Brittle fracture and the brittle-to-ductile transition of tungsten. J. Nucl. Mater. **323**, 304–312 (2003)

22. A.S. Argon, S.R. Maloof, Plastic deformation of tungsten single crystals at low temperatures. Acta Metall. **14**, 1449–1462 (1966)

23. P. Beardmore, D. Hull, Deformation and fracture of tungsten single crystals. J. Less Common Metals **9**, 168–180 (1965)

24. R.M. Rose, D.P. Ferriss, J. Wulff, Yielding and plastic flow in single crystals of tungsten. Trans. Met. Soc. AIME **224**, 981–990 (1962)

25. J. Riedle, P. Gumbsch, H. Fischmeister, Cleavage anisotropy in tungsten single crystals. Phys. Rev. Lett. **76**, 3594–3597 (1996)

26. D. Rupp, S.M. Weygand, Anisotropic fracture behaviour and brittle-to-ductile transition of polycrystalline tungsten". Philos. Mag. **90**, 4055–4069 (2010)

27. J. Reiser, M. Rieth, A. Möslang, B. Dafferner, A. Hoffmann, X. Yi, D. Armstrong, Tungsten foil laminate for structural diverter applications: tensile test properties of tungsten foil. J. Nucl. Mater. **434**, 357–366 (2013)

28. D. Rupp, *Bruch Und Spröd-Duktil-Übergang in Polykristallinem Wolfram: Einfluss von Mikrostruktur Und Lastrate* (Shaker Verlag, Dueren, 2010).

29. A. Leitner, V. Maier-Kiener, D. Kiener, Dynamic nanoindentation testing: is there an influence on a material's hardness? Mater. Res. Lett. **5**, 486–493 (2017)

30. D.E. Stegall, M.A. Mamun, B. Crawford, A. Elmustafa, Indentation size effect in fcc metals: an examination of experimental techniques and the bilinear behavior. J. Mater. Res. **27**, 1543 (2012)

31. G.M. Pharr, J.H. Strader, W. Oliver, Critical issues in making small-depth mechanical property measurements by nanoindentation with continuous stiffness measurement. J. Mater. Res. **24**, 653–666 (2009)

32. B. Merle, V. Maier-Kiener, G.M. Pharr, Influence of modulus-to-hardness ratio and harmonic parameters on continuous stiffness measurement during nanoindentation. Acta Mater. **134**, 167–176 (2017)

33. M. Rester, C. Motz, R. Pippan, The deformation-induced zone below large and shallow nanoindentations: a comparative study using EBSD and TEM. Phil. Magn. Lett. **88**, 879–887 (2008)

34. M. Rester, C. Motz, R. Pippan, Indentation across size scales-a survey of indentation-induced plastic zones in copper {1 1 1} single crystals. Scripta Mater. **59**, 742–745 (2008)

35. M. Rester, C. Motz, R. Pippan, Where are the geometrically necessary dislocations accommodating small imprints? J. Mater. Res. **24**, 647–651 (2009)

36. M. Rester, C. Motz, R. Pippan, Microstructural investigation of the volume beneath nanoindentations in copper. Acta Mater. **55**, 6427–6435 (2007)

37. E. Demir, D. Raabe, N. Zaafarani, S. Zaefferer, Investigation of the indentation size effect through the measurement of the geometrically necessary dislocations beneath small indents of different depths using EBSD tomography. Acta Mater. **57**, 559–569 (2009)

38. F. Javaid, Y. Xu, E. Bruder, K. Durst, Indentation size effect in tungsten: quantification of geometrically necessary dislocations underneath the indentations using HR-EBSD. Mater. Charact. **142**, 39–42 (2018)

39. J. Wang, L. Luan, T. Volz, S.M. Weygand, R. Schwaiger, Size-dependent geometrically necessary dislocation structures in single-crystalline tungsten. Submitted (2021)

40. J. Hirth, J. Lothe, *Theory of Dislocations*, 2nd edn. (Wiley, New York, 1982).

41. A. Argon, *Strengthening mechanisms in crystal plasticity*. Oxford University Press on Demand (2008)

42. N.J.V. Schmitt, Experimentelle Untersuchung des Verformungs- und Bruchverhaltens von Ein-, Bi- und Polykristallinem Wolfram auf der Mikroskala (Karlsruhe Institute of Technology, 2016), http://digbib.ubka.uni-karlsruhe.de/volltexte/1000062471

43. M. Cordill, N. Moody, W. Gerberich, Effects of dynamic indentation on the mechanical response of materials. J. Mater. Res. **23**, 1604–1613 (2008)

44. B. Lucas, W. Oliver, Indentation power-law creep of high-purity indium. Metall. Mater. Trans. A **30**, 601–610 (1999)